Journal of Materials Chemistry A

ROYAL SOCIETY OF CHEMISTRY

PAPER

View Article Online
View Journal | View Issue

Check for updates

Cite this: J. Mater. Chem. A, 2026, 14, 11284

High temperature grain boundary resistance in $Yb_{14}(Mg,Mn)Sb_{11}$ thermoelectrics

Duncan Zavanelli, [a] Eleonora Isotta, [ab] Florian Busch, [b] Siyuan Zhang, [b] Christina Scheu, [b] Sabah Bux [c] and G. Jeffrey Snyder *[a]

Grain boundary electrical resistance has been a limiting factor in the thermoelectric performance of many otherwise promising materials. For example, the recent emergence of Mg_3Sb_2 as a high performing low temperature thermoelectric material is a result of efforts to mitigate grain boundary electrical resistance. Many other materials including half Heuslers, oxides, Mg_2Si and others have also seen improved thermoelectric performance after mitigating grain boundary electrical resistance. However, the focus of grain boundary engineering work has been on low and mid temperature materials. Grain boundary electrical resistance is typically strongest at room temperature, so it has been assumed that high temperature thermoelectrics do not need to be evaluated for detrimental grain boundary electrical resistance. In this study, we demonstrate the importance of grain boundary resistance in all temperature ranges by discovering large grain boundary resistance in the high temperature thermoelectric $Yb_{14}MgSb_{11}$. While the observed boundary resistance is still largest at room temperature, there is still significant boundary resistance in the measured temperature range. As a result, a 22% increase in thermoelectric figure of merit is acheived at 1000 °C by increasing the grain size. Further, we demonstrate the importance of bulk composition to grain boundary engineering, as substituting Mg for Mn completely removed all measurable grain boundary resistance. These results demonstrate that grain boundary resistance is important in all thermoelectric materials regardless of targeted operating temperature.

Received 19th November 2025
Accepted 3rd February 2026

DOI: 10.1039/d5ta09385f

rsc.li/materials-a

1 Introduction

Thermoelectric materials can be used to convert temperature gradients into electrical power with no moving parts and limited performance degradation over time. This makes thermoelectric generators good candidates for space missions when solar cells are not possible. They are used in Radioisotope Thermoelectric Generators (RTGs) deployed in several NASA missions, including the Mars rovers Perseverance and Curiosity.[1–3] The hot side temperature of thermoelectric devices in RTGs can exceed 1000 °C, so thermoelectric materials optimized for high temperature performance are needed to fully utilize the provided heat.[4,5]

Zintl based thermoelectrics have emerged as promising candidates for high temperature RTG applications. Zintl compounds have highly tunable electronic structures,[6] combined with very complicated crystal structures characterized by complicated poly-anion frameworks.[7,8] In particular, compounds with the stoichiometry $Yb_{14}(Mn,Mg)Sb_{11}$ have emerged as high performing materials at 1000 °C.[9,10] Thermoelectric performance is evaluated using the material figure of merit $zT = \frac{\sigma S^2}{\kappa} T$ where σ is the electrical conductivity, S is the Seebeck coefficient, and κ is the thermal conductivity. $Yb_{14}(Mn,Mg,Zn)Sb_{11}$ materials have been found to reach zTs over 1 at 1000 °C, demonstrating their promise for RTG applications. Efforts to improve these materials have included compositing with W and Fe to improve mechanical stability and electrical conductivity.[11,12] Despite these attempts to control and improve the microstructure of these materials, there have been no studies on the impact of grain boundaries on their thermoelectric performance.

Grain boundaries have been shown to have a large detrimental impact on thermoelectric performance, particularly through large added electrical resistance.[13,14] The added resistance from grain boundaries has been described as a buildup of charge in a space-charge region, similar to a n–p junction or Schottky barrier, as the boundary region will have a different concentration of charged defects than the bulk.[15] Recent work on half Heusler materials has demonstrated that altering the boundary composition can change or eliminate the charge barrier.[16–18] These charged barriers result in large boundary

[a]Northwestern University, Department of Materials Science and Engineering, Evanston, IL 60208, USA. E-mail: jeff.snyder@northwestern.edu

[b]Max Planck Institute for Sustainable Materials, Max-Planck-Straße 1, Düsseldorf, 40237, Germany

[c]Photovoltaic, Electrochemical and Thermoelectric Systems Group, Jet Propulsion Laboratory/California Institute of Technology, Pasadena, CA 91109, USA

resistance at room temperature that decays exponentially at higher temperatures. An equation for conductivity in materials where conductivity is dominated by charged boundary resistance is presented by Hu *et al.*:[13]

$$\rho_{GB} = \frac{1}{e^2 dn}\left(\frac{1}{2\pi m^* k_B T}\right)^{-1/2} \exp\left(\frac{E_b}{k_B T}\right) \quad (1)$$

where ρ_{GB} is the resistivity from grain boundaries, d is the grain size, n is the carrier concentration, m^* is the charge carrier effective mass and E_b is the height of the potential barrier in the space-charge region.

However, directly applying this equation to bulk thermoelectric materials is difficult, as highly doped semiconductors can have strong contributions from both grain boundary resistance and bulk scattering mechanisms. As a result, E_b values calculated from eqn (1) are often misleading. As an example, $Nb_{0.95}Ti_{0.05}FeSb$ has strong grain boundary resistance despite the lack of exponential behavior observable in conductivity.[17,19] In order to model or explain grain boundary behavior in conductive materials, it is necessary to first separate the grain boundary and grain contributions to total resistivity.

This can be achieved through a two-phase or "brick-layer" model, where polycrystalline materials are treated as a two phase material, with one phase (grain boundaries) wrapped around the other (the bulk).[20] A schematic of this is shown in Fig. 1a, where the red arrow represents the charge transport path. It is assumed that the grain boundaries are much more resistive than the bulk, so all transport should follow this path. This results in a series circuit between the grain and grain boundary phases. In previous studies, this series circuit was used along with a grain boundary width to calculate grain boundary resistivity. However, the width of a grain boundary is both hard to define and measure. To remove this limitation, an excess resistance approach was proposed by Zavanelli *et al.*[16] This approach is shown in Fig. 1b, where the excess resistance is a 2D added resistance integrating the total added resistance from boundaries. This results in the following equation:

$$\rho^{-1} = \rho_G{}^{-1} + \frac{1}{d} R_{GB} \quad (2)$$

where ρ_G is the grain resistivity and R_{GB} is the excess grain boundary resistance. This equation can be used to easily calculate both grain and boundary properties from samples with different grain sizes and similar carrier concentrations. This is illustrated in Fig. 1c, where the slope of the ρ *vs.* $1/d$ line is the excess resistance and the x intercept is the grain resistivity.

The exponential decay of this resistance as a function of temperature has resulted in most grain boundary resistance mitigation efforts being targeted at room and mid temperature thermoelectric materials. For example, Mg_3Sb_2,[21–23] oxide thermoelectrics,[24] half Heuslers,[19,25–27] rare earth tellurides[28] and many others. However, multiple recent studies have suggested that boundary resistance is also important in high temperature materials. Boundaries showing a metallic resistance that increases with temperature, $\rho_{GB} \propto T$, were demonstrated in La_3Te_4.[29] In addition, boundaries that are more conductive than bulk grains have been demonstrated in Ti(Co,Fe)Sb.[30]

Both $Yb_{14}MgSb_{11}$ and $Yb_{14}MnSb_{11}$ also show signs of grain boundary resistance in their reported resistivity.[31,32] They show a change in the temperature dependence of conductivity near room temperature, which is common evidence of grain boundary resistance. Given this temperature activated conductivity behavior and the recent work suggesting the importance of grain boundaries even at high temperature, characterization of the grain boundary resistance in these materials is needed.

In this study, we evaluate the impact of microstructure and grain boundary resistance on the thermoelectric performance of $Yb_{14}MgSb_{11}$ and $Yb_{14}MnSb_{11}$ by controlling grain size. Changing the hot pressing temperature results in a series of samples with larger grain sizes as pressing temperature increases. From these samples, we identify strong grain boundary resistance in $Yb_{14}MgSb_{11}$, with the largest grain size resulting in the best performance. However, we also observe that this grain boundary resistance is still significant at the highest measured temperature, 1000 °C. This demonstrates that despite the decrease in grain boundary resistance with temperature, charged boundary resistance should not be neglected in high temperature thermoelectrics.

In contrast, no grain boundary resistance is measurable in $Yb_{14}MnSb_{11}$ despite a large change in grain size. This demonstrates the importance of using bulk composition to tailor grain boundary properties.

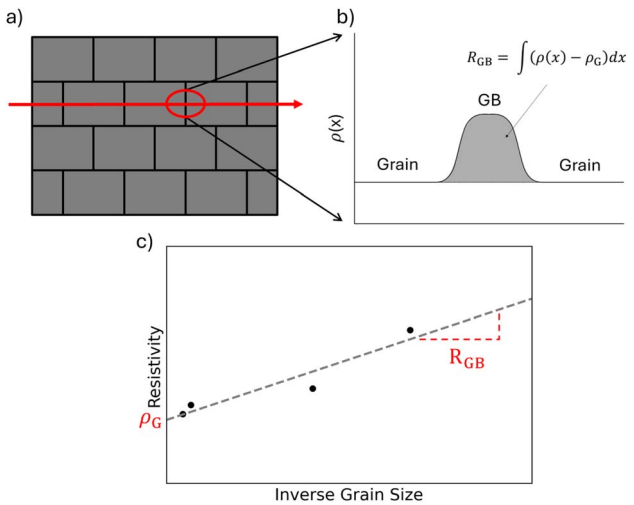

Fig. 1 (a) Schematic of the brick-layer or two phase model for electrical conductivity in polycrystalline materials, where the gray "bricks" represent grains and the black "mortar" represents the boundaries. (b) Included is another schematic for demonstrating how the added resistance from grain boundaries can be treated as a 2D boundary resistance. (c) A demonstration of how to calculate R_{GB} and ρ_G from bulk resistivity and grain size.

2 Methods

2.1 Synthesis

$Yb_{14}MgSb_{11}$ and $Yb_{14}MnSb_{11}$ were both synthesized through ball milling and hot pressing approach similar to that described in Borgsmiller *et al.*[33,34]

For synthesizing $Yb_{14}MgSb_{11}$, Mg shot (99.9%, Alfa Aesar) and Sb were ball milled for 2 hours with an intermediate scraping step to form Mg_3Sb_2 as a precursor. From previously published results,[34] a 20% excess of Mg was used to counter Mg losses during the ball milling process. The obtained Mg_3Sb_2 was then combined with Yb shavings and Sb shot (99.999% 5N Plus) in the stoichiometry Yb: 14.02, Mg_3Sb_2: 0.4, Sb: 10.2 to give $Yb_{14}MgSb_{11}$ with a small Mg and Yb excess to account for further losses during ball milling.[32] This composition was ball milled for a further 3 hours with a scraping step every hour to mitigate Yb and Mg agglomeration.

To synthesize $Yb_{14}MnSb_{11}$, Mn chunks were first purified by heating in a quartz tube with quartz wool at 1000 °C to remove oxide. Mn was then combined with Sb to form MnSb by combining the purified Mn with Sb shot in a quartz tube and heating to 1000 °C and holding for two hours. The temperature was then lowered to 675 °C and held for 48 hours before being air quenched. This MnSb was then combined with Yb and Sb with 5% excess Mn and underwent a similar ball milling procedure as $Yb_{14}MgSb_{11}$

Bulk pollycrystalline pellets of both compositions were obtained using a hot press with a pressure of 80 MPa with temperatures ranging from 1050 °C to 1300 °C for 80 minutes.

2.2 Thermoelectric property measurements

Temperature dependent electronic conductivity was measured in a high vacuum Hall setup. Measurements were done using four point probes with the van der Pauw method.[35]

Seebeck coefficients were measured using a home built system with the light pulse method and measured with W–Nb Thermocouples under high vacuum.[36]

Thermal transport measurements were using a Netzsch LFA 457 MicroFlash instrument to measure thermal diffusivity. The density was measured at room temperature using the Archimedes method, and then corrected for thermal expansion using reported values of the coefficient of thermal expansion.[37] The heat capacity used was based on reported values.[31]

2.3 X-ray diffraction

XRD data were collected at room temperature on a STOE-STADI-MP diffractometer equipped with an asymmetric curved Germanium monochromator (Cu Kα1 radiation, $\lambda = 1.5406$ Å). The line-focused Ag X-ray tube was operated at 40 kV and 40 mA. Data was collected in reflection mode.

For higher resolution scans presented in the SI, Ag Kα1 radiation $\lambda = 0.559407$ Å was used.

2.4 Electron microscopy

Bright field Scanning transmission electron microscopy (STEM) and Energy Dispersive X-ray Spectroscopy (EDS) were conducted on a Jeol 2100 microscope operated at 200 kV using a camera length of 40 cm. Lamellae for STEM and EDX were prepared using Ga^+ focused ion beam (FIB) in a Scios2 dual beam microscope, according to the procedure in ref. 38. STEM-EDS spectrum imaging datasets were processed by multivariate statistical analysis[39] to reduce noise and differentiate X-ray emission from secondary phases.

2.5 Hardness testing

Hardness was tested using the Vickers indentation method and performed with a Wilson VH 3100 hardness tester. Indentations were measured using an integrated optical microscope. Prior to measurement, samples were polished to a 1 μm finish using a water-free Al_2O_3 suspension. A load of 1.96 N and contact time of 10 s were chosen based on the results of Ceretti *et al.*[12] The load chosen was based on the smallest load where hardness was roughly load-independent. Higher loads significantly increased spalling and the rate of unusable indentations.

3 Results and discussion

3.1 Microstructure

In order to identify grain boundary resistance in thermoelectric materials, a series of samples with different grain sizes must be synthesized. There are multiple possible methods to achieve this, including changing starting powder size, ball milling time, and sintering temperature. For this work, the hot pressing sintering temperature was changed. This approach has been demonstrated to produce large changes in grain size with pressing temperature in many thermoelectric materials.[17,19,29] This approach also minimizes other possible changes to the material as hot pressed powder is typically fully reacted. Samples pressed at 1050 °C, 1150 °C, 1250 °C, and 1300 °C were synthesized. In addition, two samples of $Yb_{14}MnSb_{11}$ were pressed at 1050 °C and 1250 °C to determine if there was a difference in grain boundary behavior.

In order to evaluate the success of our approach in producing a series of samples with different grain sizes but same phase

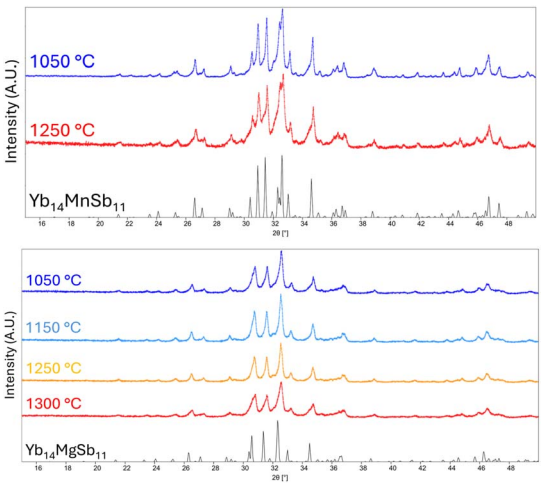

Fig. 2 X-ray diffraction spectra for (top) $Yb_{14}MnSb_{11}$ and (bottom) $Yb_{14}MgSb_{11}$ collected with Cu $K\alpha_1$ radiation. The reference pattern for $Yb_{14}MnSb_{11}$ was retreived from the Materials Project database.[40] The reference pattern for $Yb_{14}MgSb_{11}$ was generated using the reported structure data from Hu *et al.*[10] There are no impurity peaks present in samples of either material, and neither display differences in XRD pattern with pressing temperature.

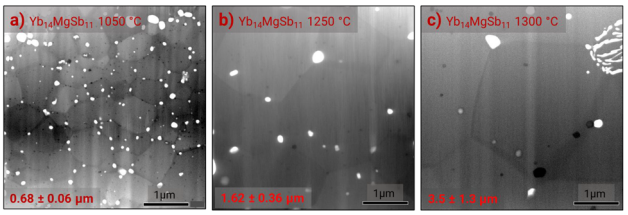

Fig. 3 Scanning Transmission Electron Microscopy (STEM) imaging of $Yb_{14}MgSb_{11}$ pressed at (a) 1050 °C, (b) 1250 °C, and (c) 1300 °C. For both $Yb_{14}MgSb_{11}$ and $Yb_{14}MnSb_{11}$, grain size increased with pressing temperature.

purity, X-ray diffraction (XRD) patterns for both $Yb_{14}MnSb_{11}$ and $Yb_{14}MgSb_{11}$ are shown in Fig. 2. From the XRD data, there are no major differences between samples of the same material pressed at different temperatures. All of the synthesized samples also match the reported structure for either $Yb_{14}MgSb_{11}$ or $Yb_{14}MnSb_{11}$.[10,40] However, it is also important to note that the Yb–Mg–Sb and Yb–Mn–Sb phase diagram is very complex in the region around the 14–1–11 composition, with many other complex crystal phases with similar structures, such as $Yb_{10}MgSb_9$,[34] $Yb_{11}Sb_{10}$,[41] and $Yb_{21}Mg_4Sb_{18}$.[42] Borgmsiller *et al.* demonstrated that differentiating these secondary phases from XRD alone is difficult, especially when multiple of these phases are present.[41] Higher resolution XRD patterns were obtained with Ag-Ka1 radiation and are presented in Fig. S1 for the samples pressed at 1050 °C and 1250 °C. These scans further demonstrate that there is no observable change in secondary phase content between samples pressed at different temperatures. In addition, the similar measured carrier concentrations and Seebeck coefficients shown in Fig. 4b between pressing temperatures supports that all have analogous phase purity and secondary phase content. Thus any change in properties between samples can not be explained by different impurity contents caused by changing the hot pressing temperature.

In order to confirm that the grain size of $Yb_{14}MgSb_{11}$ and $Yb_{14}MnSb_{11}$ increased with pressing temperature, the grain sizes of selected samples were measured with STEM. $Yb_{14}MgSb_{11}$ samples with three different pressing temperatures were measured and the results are shown in Fig. 3. Using this approach, grain size was demonstrated to increase with pressing temperature in line with expected behavior. The grain size of the 1050 °C pressed samples was 0.68 ± 0.06 µm, the 1250 °C sample had a grain size of 1.62 ± 0.36 µm, and the 1300 °C sample had a grain size of 3.5 ± 1.3 µm. These grain sizes were obtained using a mean intercept approach, and a more detailed breakdown of the grain size measurements is presented in Fig. S2. The grain sizes of $Yb_{14}MnSb_{11}$ pressed at 1050 °C and 1250 °C were measured to be 0.87 ± 0.15 µm and 6.4 ± 1.3 µm respectively, with STEM images shown in Fig. S3.

We note that, besides the diffraction contrast arising from the different grains, STEM images exhibit some darker and brighter spots. Energy Dispersive X-ray Spectroscopy shown in Fig. S4 attributes the darker spots to Yb enrichment. Although some of the bright spots are pores, which in part may have formed during the lamella preparation procedure, others are attributed to Mg segregation. These are particularly evident in the sample pressed at 1300 °C and probably arise from the Mg-rich synthesis conditions. In contrast, the Mn samples do not show any similar Mn precipitates.

In addition to changing grain size, increasing the hot pressing temperature can also impact sample densities. The densities for the $Yb_{14}MnSb_{11}$ samples were measured using the Archimedes method to be 8.10, 8.12, 8.19, and 8.20 g cm^{-3} for the 1050 °C, 1150 °C, 1250 °C, and 1300 °C samples. The measured densities of the $Yb_{14}MnSb_{11}$ samples were 8.16 and

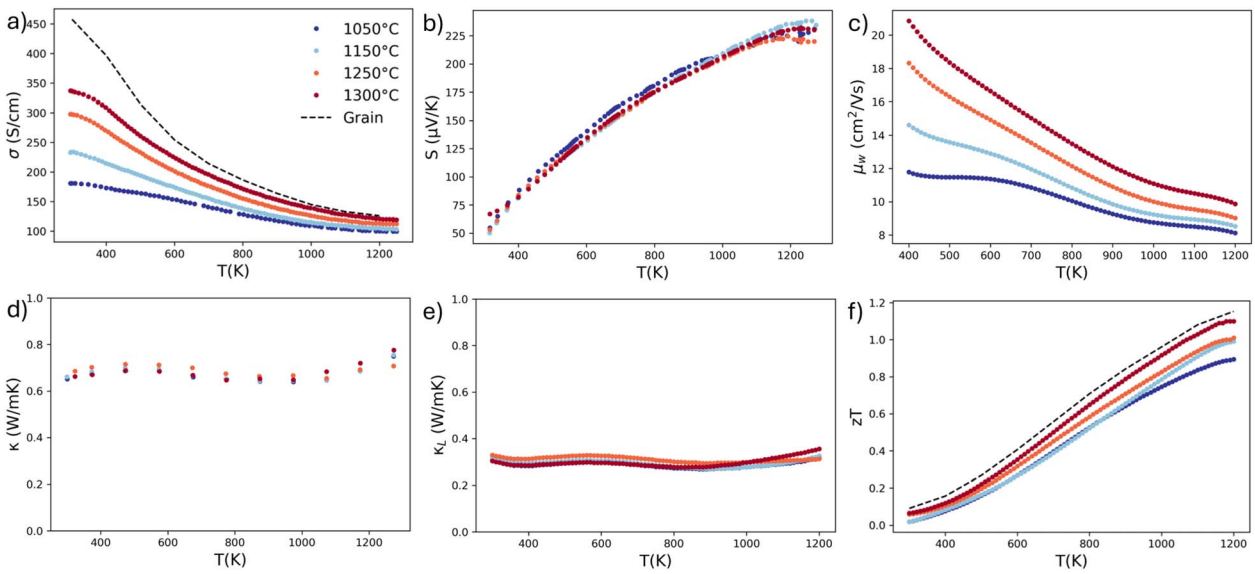

Fig. 4 Measured thermoelectric transport properties of $Yb_{14}MgSb_{11}$ samples with four different pressing temperatures. The (a) electrical conductivity, (b) Seebeck coefficient, (c) calculated weighted mobility, (d) thermal conductivity, (e) calculated lattice thermal conductivity using the modified form of the Wiedemann–Franz law proposed by Kuo *et al.*,[43] and (f) thermoelectric figure of merit zT are shown here. The calculated values for grain conductivity and zT are calculated in the following section.

8.18 g cm^{-3} for the 1050 °C and 1250 °C samples. While the densities do increase with pressing temperature, the increase is too small to explain any large changes in transport properties.

3.2 Thermoelectric transport

The thermoelectric transport properties for the four $Yb_{14}MgSb_{11}$ samples pressed at 1050 °C, 1150 °C, 1250 °C, and 1300 °C are shown in Fig. 4. The most immediate difference between the samples is in the electrical conductivity, shown in Fig. 4a. Increasing the pressing temperature and thus grain size resulted in an increase in conductivity for all samples. The change in conductivity is largest at room temperature, with an increase of 86% from 181 S cm^{-1} to 337 S cm^{-1} between the 1050 °C and 1300 °C sample. Importantly, there is still a change in conductivity even at high temperature, with an increase of 19% from 100 S cm^{-1} to 119 S cm^{-1} at 1000 °C. Qualitatively, this change in conductivity with grain size follows the charged boundary behavior from eqn (1). This result is unusual in that there is still a large difference in conductivity at 1000 °C despite the exponential decay of boundary resistance with temperature.

However, before this change in conductivity can be ascribed to grain boundary electrical resistance, it is important to eliminate other possible factors. Bulk electrical transport properties are often sensitive to the synthesis parameters, as they can affect defect concentrations and material dopability. For example changing ball milling time in TiNiSn has been shown to change carrier concentration.[26] In order to eliminate this possibility, the Seebeck data is useful as it is primarily a bulk measurement. The Seebeck data for each sample is shown in Fig. 4b. The Seebeck data between each sample is roughly constant within the expected error of Seebeck measurements.[44] Since the Seebeck coefficient is dependent on material Fermi level, a constant Seebeck indicates that the doping level in all samples should be similar. In addition, the Hall carrier concentrations were measured and are reported in Fig. S5. The sample pressed at 1300 °C has a slightly higher carrier concentration of 5.6×10^{20} as compared to 4.7×10^{20} observed in the samples pressed at lower temperatures. However, this small change in carrier concentration is insufficient to explain the large increase in conductivity and different temperature dependence.

In order to further confirm that the small fluctuations in Seebeck and carrier concentration between samples can not explain the change in conductivity, the weighted mobility is calculated and shown in Fig. 4c. The weighted mobility is independent of carrier concentration, so any changes to weighted mobility between these samples will be the result of grain boundary resistance. The weighted mobilities follow a very similar trend to the conductivity, with a large increase with grain size at room temperature and a smaller but still significant increase at 1000 °C.

In addition to this trend, all four samples show a weighted mobility trend that does not follow that expected for single parabolic band materials. In particular, the kink in weighted mobility at 1000 K is unexpected, while that at 600 K in the 1050 °C and 1150 °C samples is expected from the grain boundary resistance. This kink is a result of the multi-band transport that occurs in $Yb_{14}MgSb_{11}$, where a second heavy hole band influences transport at high temperature.[32] To confirm that the kink is a result of the multi band transport, the measured Seebeck and carrier concentration for all samples are compared to predicted Pisarenko plots calculated with a single parabolic model and multiband model by Perez *et al.*[32] The resulting relation is shown in Fig. S6, where the measured Seebeck is much higher than predicted by a single parabolic band. This effect is stronger at higher temperatures as more of the second conduction band is activated, resulting in a larger than expected high temperature weighted mobility.

The measured thermal conductivity and calculated lattice thermal conductivity are shown in Fig. 4d and e. Despite the large change in grain size, there is no observable change in total thermal conductivity. This is likely a result of the low intrinsic thermal conductivity of $Yb_{14}MgSb_{11}$ owing to its large and complicated unit cell. Similarly to the weighted mobility, the effect of the multi-band transport can be observed in the increase of thermal conductivity after 900 K.

The lattice thermal conductivity was calculated using a modified form of the Wiedemann Franz Law, $\kappa_L = \kappa - L\sigma_G T$, where L is the Lorenz number and σ_G is the grain conductivity.[43,45,46] This modification is necessary because the electronic thermal transport from electrons inside a grain should not be dependent on the electronic conductivity of a grain boundary. Using the measured conductivity in a material with grain boundary resistance results in overestimation of the lattice thermal conductivity, where higher boundary resistance results in higher κ_L. This gives an unphysical result where larger grain sizes result in lower calculated lattice thermal conductivity. Instead, a two phase model can be used, where thermal conductivity can be represented by a circuit with a grain and boundary phase in series, each with a lattice and electronic component. In materials with resistive boundaries, $\kappa_{e,GB}$ will be approximately zero. This results in the equation $\kappa^{-1} = (1 - f_{GB})(\kappa_{L,G} + \kappa_{e,G})^{-1} + f_{GB}\kappa_{L,GB}^{-1}$ where f_{GB} is the volume fraction of grain boundaries. Given that the measured thermal conductivity in $Yb_{14}MgSb_{11}$ is almost constant across a large range of grain sizes, it is unlikely the boundaries are thermally resistive, so we can neglect $\kappa_{L,GB}$ in this case. This results in $\kappa_L = \kappa - L\sigma_G T$. The values of σ_G used for this calculation are shown in Fig. 4a.

To demonstrate that this modification is needed, κ_L was also calculated for $Yb_{14}MgSb_{11}$ using the standard Wiedemann Franz law. This calculation results in a 27% decrease in κ_L as grain size increases, with κ_L decreasing from 0.52 to 0.39 W mK^{-1} between the 1050 °C and 1300 °C samples. The full κ_L *versus* temperature for all samples calculated with $L\sigma T$ is shown in Fig. S7. In addition, a comparison of the uncertainty in κ_L in both methods for the 1050 °C sample is shown in Fig. S8, using uncertainty values from Heremans *et al.*[44] and Borup *et al.*[47]

To further illustrate this point, κ_L *versus* inverse grain size is shown in Fig. 5 with both versions of the Wiedemann Franz law. This plot demonstrates not only how the lattice thermal conductivity increases as grain size decreases when using the standard approach, but also how the grain κ_L is overestimated. Using grain conductivity instead predicts values of κ_L that are

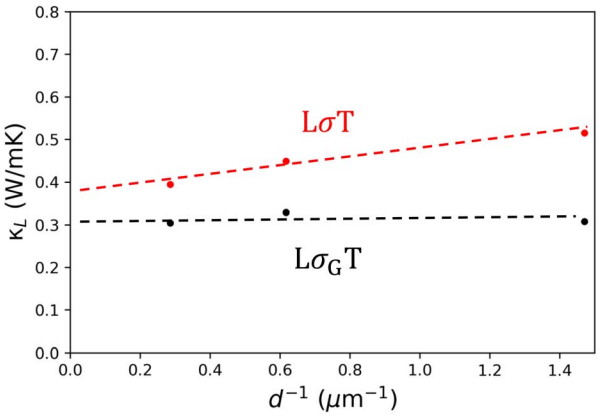

Fig. 5 Lattice thermal conductivity *versus* inverse grain size for $Yb_{14}MgSb_{11}$ samples calculated with the standard (red) and revised (black) version of the Wiedemann Franz law. The *y* intercept represents the grain value of κ_L.

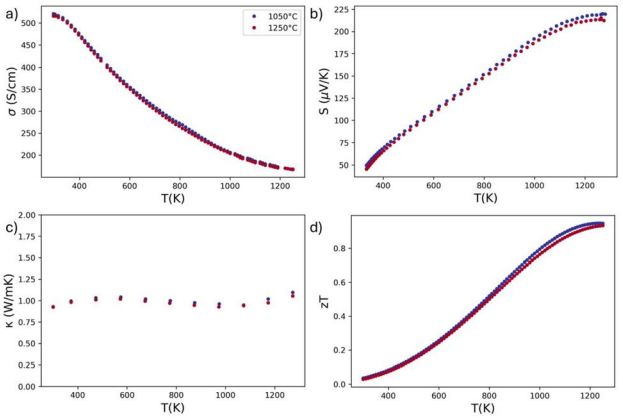

Fig. 6 Theremoelectric transport properties of $Yb_{14}MnSb_{11}$ with two different pressing temperatures and grain sizes. Shown are the (a) electrical conductivity, (b) Seebeck coefficient, (c) thermal conductivity, and (d) *zT*.

independent of the electronic resistance from boundaries. This is needed particularly in materials where grain boundaries are both thermally and electronically resistive, as estimating the thermal boundary resistance is impossible if it is countered by a lower measured conductivity. Further, reliable estimates of lattice thermal conductivity are needed for analyzing the material quality factor ($B \propto \mu_w/\kappa_L$),[48] as the standard Wiedemann Franz law underestimates *B* in all materials with electronic boundary resistance.

However, this approach still assumes that the lattice thermal conductivity is homogeneous in a polycrystalline material. As recent studies using Frequency Domain Thermoreflectance (FDTR) have demonstrated, this assumption is not always correct.[49,50] In those cases, it would be necessary to introduce additional κ_G and κ_{GB} terms. Using $\kappa_L = \kappa - L\sigma_G T$, all three samples have similar lattice thermal conductivities.

With the conductivity, Seebeck, and thermal conductivity, *zT* was calculated in Fig. 4f. With a constant Seebeck and thermal conductivity, the increase in conductivity with grain size resulted in a *zT* that also increase with grain size. This increase in *zT* is maintained even at 1000 °C, with an increase of 22% from 0.92 with a 0.68 μm grain size to 1.12 with a 3.5 μm grain size. This increase in high temperature performance demonstrates that charged boundary resistance can still be important at high temperatures despite the $\exp\left(\frac{-E_b}{k_B T}\right)$ term in eqn (1). This result demonstrates that grain boundary resistance is important to thermoelectric materials regardless of their operating temperature.

To test the impact of composition on the grain boundary resistance of $Yb_{14}MgSb_{11}$, two samples of $Yb_{14}MnSb_{11}$ were also synthesized and measured with their electrical conductivity, Seebeck, thermal conductivity, and *zT* shown in Fig. 6. Despite the large change in grain size between these two samples from 0.87 μm to 6.4 μm, there was no change in measured properties.

These results indicate the lack of any electrical or thermal boundary resistance in $Yb_{14}MnSb_{11}$, in contrast with the large electrical boundary resistance in $Yb_{14}MgSb_{11}$. The higher electrical boundary resistance in $Yb_{14}MgSb_{11}$ is a result of both the addition of Mg and change in synthesis parameters. Mg based compounds often have large grain boundary resistance, attributed to Mg vacancies found at grain boundaries, like in the material Mg_3Sb_2.[51] Other Mg-based zintl materials have also demonstrated possible grain boundary resistance alongside Mg vacancies, such as $BaMg_2Sb_2$ and $EuMg_2Sb_2$.[52] These vacancies can be mitigated by introducing Mg after the sintering process,[21] but excess Mg introduced prior to sintering increases boundary resistance in $Mg_2(Sn,Si)$.[53] Ghosh *et al.* demonstrated that Mg loss occurs primarily through diffusion of Mg from the boundaries to the surface, indicating that there is likely Mg deficiency in grain boundaries even in Mg rich materials.[54] This suggests that the grain boundary resistance is a result of Mg depletion in both Mg rich and Mg poor materials. The detrimental effects of Mg are potentially exacerbated in the case of $Yb_{14}MgSb_{11}$, as excess Mg was used during the synthesis process to combat losses from ball milling relatively soft metals and to avoid the detrimental $Yb_{11}Sb_{10}$ secondary phase.[33]

The sensitivity of grain boundary resistance to bulk composition has been observed in other thermoelectric materials, particularly in $Nb_{1-x}Ti_xFeSb$[16,17] and Ti(Co,Fe)Sb[30] where changing the Ti and Fe content respectively changed the composition at the boundary. The result shown here where switching the highly reactive Mg for the more stable Mn mitigates boundary scattering further emphasizes the importance of using bulk composition to tailor microstructure and grain boundary properties. In the case of $Yb_{14}(Mn,Mg)Sb_{11}$, there is a trade off between higher performance and *zT* in the Mg based material, and microstructure independent properties in the Mn based material.

3.3 Grain boundary behavior

With the grain size data from Fig. 3 and bulk transport measurements from Fig. 4, it is possible to model the grain boundary resistance using an excess resistance approachas described in Fig. 1c. The advantage of this approach over other previous models, such as the two-phase model,[20] is that it does

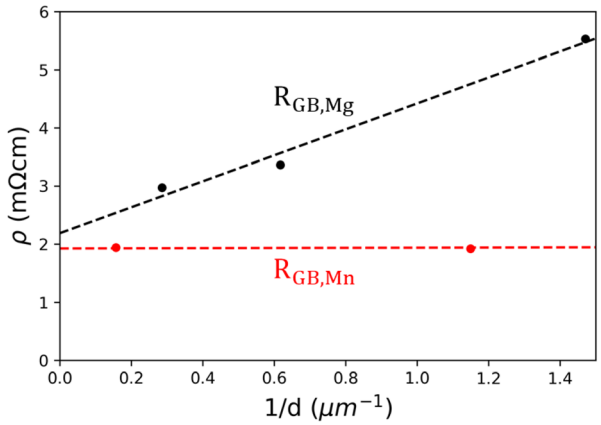

Fig. 7 Resistivity *versus* inverse grain size at 300 K for both $Yb_{14}MgSb_{11}$ (black) and $Yb_{14}MnSb_{11}$ (red) with the slope of the dashed lines showing R_{GB}.

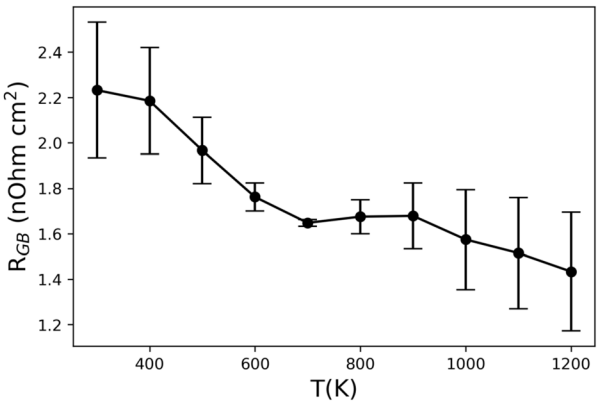

Fig. 8 Calculated excess boundary resistance, R_{GB}, in $Yb_{14}MgSb_{11}$ from eqn (2) using the grain sizes and measured conductivities for samples pressed at 1050 °C, 1250 °C, and 1300 °C.

not require any details specific to a single grain boundary. In particular, grain boundary width is problematic as it is difficult to measure, seldom reported, and difficult to define. In contrast, those parameters will all contribute to the R_{GB} measured through bulk properties. This allows easier comparison of different materials.

Using eqn (2), R_{GB} can be calculated as the slope of resistivity *versus* inverse grain size. An example of this is shown in Fig. 7 for both $Yb_{14}MgSb_{11}$ and $Yb_{14}MnSb_{11}$ at 300 K. Aside from demonstrating a R_{GB} calculation, this data also shows the effect of Mn substitution. When changing bulk composition, two possible effects can contribute to changes in observed boundary resistance. The composition change can either change the sintering behavior of a material and thus the grain size, or the composition change can make individual boundaries more or less resistive. An example of this is Nb doped Mg_3Sb_2, where Nb was first posited as sintering aid to increase grain size,[55] but has since been demonstrated to also reduce the resistance of boundaries irrespective of grain size.[23] From Fig. 7, it is clear that the main effect of switching Mg to Mn is making boundaries less resistive, not increasing grain size. Another interesting result is that the x intercept of the ρ *vs.* $1/d$ plots for both Mn and Mg compositions are approximately the same, suggesting that the grain conductivities are similar in both materials.

R_{GB} has been calculated for the whole measured temperature range in $Yb_{14}MgSb_{11}$, and the results are shown in Fig. 8. Qualitatively, the excess resistance follows eqn (1) by decreasing with temperature, suggesting that the grain boundary resistance in $Yb_{14}MgSb_{11}$ is a result of charged boundaries. However, there is an unexpected kink around 900 K where the excess resistance plateaus before decreasing further. This change in resistance corresponds to the same location of the kink in weighted mobility from Fig. 4c, and the increase in thermal conductivity in Fig. 4d. As a result, this kink in excess resistance is likely also a result of the multi-band transport in $Yb_{14}MgSb_{11}$.[32] It is also possible to use an Arrhenius relation to extract an activation energy or energy barrier using the excess resistance. However, the bump in mid temperature excess resistance makes such fits difficult for $Yb_{14}MnSb_{11}$. Fitting a temperature range of 300K–700 K below the jump in excess resistance yields an energy barrier of 10.0 meV. It is important to note that this value should not be directly compared to values calculated using eqn (1), as ρ_{GB} and R_{GB} do not necessarily have the same temperature dependence.

It would be expected that a change in activated electronic bands influences the grain boundary resistance. A simple picture of charged boundary resistance is that the charge barrier E_b in eqn (1) is a result of a difference in electron or hole chemical potential between the boundary and grain. As a result, carriers move between the bulk and boundary until the chemical potential is equal, leaving behind charged defects which are responsible for the charged barrier. Thus, anything that changes the bulk carrier chemical potential would be expected to also change the strength of the grain boundary resistance. This concept is explained in more detail in the band shift model described by Zavanelli *et al.*[16] However, that study used a single parabolic band model to evaluate transport, where a more complicated 2-band model would be needed to model the grain boundary behavior in $Yb_{14}MgSb_{11}$.

In addition to calculating R_{GB}, eqn (2) can also be used to estimate the grain value of conductivity. This is shown in Fig. 4a. From this estimation, there is still grain boundary resistance in the largest grain material. Thus, further improvements in performance could be realized by further increasing the grain size, either by increasing the pressing temperature or altering the synthesis method. The grain zT shown in 4f suggests that further zT is still possible even at high temperatures.

From the calculated grain conductivity and the lack of grain boundary resistance in $Yb_{14}MnSb_{11}$, it is evident that the change in the conductivity temperature trend near room temperature in both materials is not a result of grain boundary resistance. Instead it must indicate a change in dominant scattering. For example, a change between polar optical phonon and acoustic phonon scattering would explain this behavior.

In addition to the standard thermoelectric properties, grain boundaries also contribute to the mechanical properties of

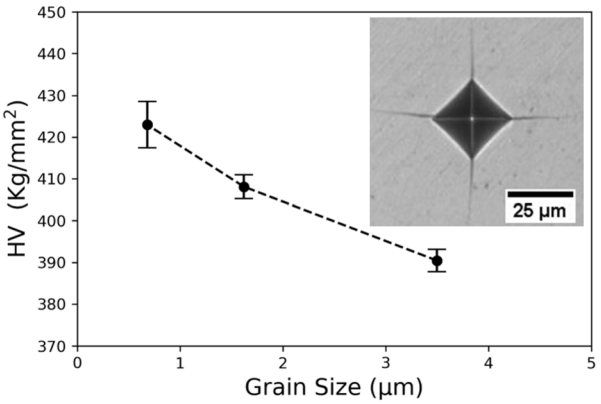

Fig. 9 Hardness values measured in the $Yb_{14}MgSb_{11}$ samples pressed at 1050 °C, 1250 °C, and 1300 °C are displayed here. These values were measured using a Vickers Micro-hardness test with an applied load of 1.96 N. The error bars correspond to the standard deviation in hardness obtained between 10 different indents for each sample. The inset shows a typical indent in the sample pressed at 1050 °C.

materials. The feasibility of thermoelectric materials in both RTGs and other thermoelectric generators or coolers is often limited by their mechanical properties.[56,57] A cracked leg will break the electrical circuit, and creep deformation can be significant given the high temperatures in RTGs.[58]

In order to evaluate the impact of grain boundaries on the mechanical stability of $Yb_{14}MgSb_{11}$, the hardness was measured and is shown in Fig. 9. These hardness values were measured using the Vickers Indentation method with an applied force of 1.96 N. This value was chosen based on previous hardness studies of $Yb_{14}MnSb_{11}$, which identified this load as the smallest load after which increasing the load further had a minimal impact on hardness.[12]

The measured hardness values for $Yb_{14}MgSb_{11}$ decreases with grain size. This trend is expected based on the Hall Petch effect, where the yield stress of a material changes with $d^{-1/2}$.[59] In the case of brittle thermoelectrics like $Yb_{14}MgSb_{11}$, it is desirable to reduce their hardness in order to improve their ductility and fracture toughness.[60] This preliminary data set demonstrates that increasing grain size is an effective way to reduce the brittleness of $Yb_{14}MgSb_{11}$. However, the impact of microstructure on the total fracture resistance of a material is complicated and includes factors such as grain shape and dislocation density.[57] Further, in some applications maximum yield strength may be a more important factor than fracture toughness, particularly in modules not designed to mitigate the high thermal stresses that can occur.[56] To determine whether fracture toughness or maximum yield stress are more important for RTG applications, a more in depth analysis of material behavior under RTG operating conditions would be required. In either case, this data demonstrates that tuning the grain size of $Yb_{14}MgSb_{11}$ is an effective method to tune mechanical properties.

The simultaneous improvement in thermoelectric properties and reduction in material brittleness demonstrates that large grain size $Yb_{14}MgSb_{11}$ should be used when possible. This also means that grain coarsening during extended operation at high temperatures is expected to improve performance.

4 Conclusions

Grain boundary resistance has been discovered in the material $Yb_{14}MgSb_{11}$ by comparing the thermoelectric transport of materials with four different grain sizes. In contrast to most examples of grain boundary resistance, this resistance was still large at high temperature, leading to a zT improvement of 22% at 1000 °C between the smallest and largest grain samples. The large effect of grain boundary resistance on performance even at 1000 °C demonstrates the importance of mitigating boundary in all thermoelectric materials regardless of operating temperature. In addition, we identified the overestimation of κ_L by 27% when using the standard Wiedemann Franz Law in $Yb_{14}MgSb_{11}$, demonstrating the importance of accounting for grain boundary resistance when calculating lattice thermal conductivities.

It was also demonstrated that substituting the oxygen sensitive and reactive Mg for the more stable Mn in $Yb_{14}MnSb_{11}$ successfully eliminates grain boundary resistance. This highlights the need to consider not only bulk properties, but also impacts on microstructure and grain boundaries when selecting bulk compositions.

Author contributions

Duncan Zavanelli: writing – original draft, investigation, formal analysis, methodology, conceptualization, data curation, validation. Eleonora Isotta: writing – review and editing, investigation. Florian Busch: writing – review and editing, investigation. Siyuan Zhang: writing – review and editing, supervision, project administration. Christina Scheu: supervision, project administration, funding acquisition. Sabah Bux: writing – review and editing, methodology, resources, supervision, funding acquisition. G. Jeffrey Snyder: writing – review and editing, conceptualization, supervision, funding acquisition, project administration.

Conflicts of interest

There are no conflicts to declare.

Data availability

The data supporting this article have been included as part of the supplementary information (SI). STEM data is available in open access at https://doi.org/10.5281/zenodo.17538066. Supplementary information is available. See DOI: https://doi.org/10.1039/d5ta09385f.

Acknowledgements

This work was performed at the Jet Propulsion Laboratory, California Institute of Technology under contract with the National Aeronautics and Space Administration. This work made use of the MatCI Facility supported by the MRSEC

program of the National Science Foundation (DMR-2308691) at the Materials Research Center of Northwestern University. This work made use of the IMSERC X-RAY facility at Northwestern University, which has received support from the Soft and Hybrid Nanotechnology Experimental (SHyNE) Resource (NSF ECCS-2025633), and Northwestern University. D. Z. was supported by a NASA Space Technology Graduate Research Opportunity. E. I. was supported by the project "MetaSCT" under HORIZON Europe: Marie Skłodowska-Curie Actions Postdoctoral Fellowships (project number 101150912). S. Z. and C. S. acknowledge funding from the German research foundation (DFG) within the Collaborative Research Centre SFB 1394 "Structural and Chemical Atomic Complexity—From Defect Phase Diagrams to Materials Properties" (Project ID 409476157).

References

1 B. Bairstow, Y. H. Lee and K. Oxnevad, *2018 IEEE Aerospace Conference*, 2018, pp. 1–19.
2 T. Tofil, T. Demichael, J. Woytach, J. Fleurial, J. Birch and S. Davis, *Proceedings of Nuclear and Emerging Technologies for Space*, NETS, 2023, pp. 268–275.
3 A. Schock, V. Sankarankandath and M. Shirbacheh, *Proceedings of the 24th Intersociety Energy Conversion Engineering Conference*, 1989, vol.6, pp. 2681–2691.
4 X. Wang, R. Liang, P. Fisher, W. Chan and J. Xu, *Renewable Sustainable Energy Rev.*, 2020, **119**, 109572.
5 M. B. R. Smith, C. Whiting and C. Barklay, *2019 IEEE Aerospace Conference*, 2019, pp. 1–11.
6 A. P. Justl, F. Ricci, A. Pike, G. Cerretti, S. K. Bux, G. Hautier and S. M. Kauzlarich, *Sci. Adv.*, 2022, **8**, eabq3780.
7 *Chemistry, Structure, and Bonding of Zintl Phases and Ions*, ed. S. M. Kauzlarich, VCH, 1996.
8 S. M. Kauzlarich, *Chem. Mater.*, 2023, **35**, 7355–7362.
9 S. R. Brown, S. M. Kauzlarich, F. Gascoin and G. J. Snyder, *Chem. Mater.*, 2006, **18**, 1873–1877.
10 Y. Hu, J. Wang, A. Kawamura, K. Kovnir and S. M. Kauzlarich, *Chem. Mater.*, 2015, **27**, 343–351.
11 C. J. Perez, X. Qi, Z. Chen, S. K. Bux, S. Chanakain, B. Li, K. Liu, R. Dhall, K. C. Bustillo and S. M. Kauzlarich, *ACS Appl. Energy Mater.*, 2020, **3**, 2147–2159.
12 G. Cerretti, O. Villalpando, J.-P. Fleurial and S. K. Bux, *J. Appl. Phys.*, 2019, **126**, 175102.
13 C. Hu, K. Xia, C. Fu, X. Zhao and T. Zhu, *Energy Environ. Sci.*, 2022, **15**, 1406–1422.
14 T. Kanno, H. Tamaki, H. K. Sato, S. D. Kang, S. Ohno, K. Imasato, J. J. Kuo, G. J. Snyder and Y. Miyazaki, *Appl. Phys. Lett.*, 2018, **112**, 033903.
15 J. Y. W. Seto, *J. Appl. Phys.*, 1975, **46**, 5247–5254.
16 D. Zavanelli, R. B. Villoro, R. H. Naderloo, N. P. Rodriguez, S. Zhang, R. He, C. Scheu and G. J. Snyder, *Phys. Rev. Mater.*, 2025, **9**, 045402.
17 R. Bueno Villoro, D. Zavanelli, C. Jung, D. A. Mattlat, R. Hatami Naderloo, N. Pérez, K. Nielsch, G. J. Snyder, C. Scheu, R. He and S. Zhang, *Adv. Energy Mater.*, 2023, **13**, 2204321.
18 R. Bueno Villoro, R. Hatami Naderloo, D. A. Mattlat, C. Jung, K. Nielsch, C. Scheu, R. He and S. Zhang, *Mater. Today Phys.*, 2023, **38**, 101240.
19 R. He, D. Kraemer, J. Mao, L. Zeng, Q. Jie, Y. Lan, C. Li, J. Shuai, H. S. Kim, Y. Liu, D. Broido, C. W. Chu, G. Chen and Z. Ren, *Proc. Natl. Acad. Sci. U. S. A.*, 2016, **113**, 13576–13581.
20 J. J. Kuo, S. D. Kang, K. Imasato, H. Tamaki, S. Ohno, T. Kanno and G. J. Snyder, *Energy Environ. Sci.*, 2018, **11**, 429–434.
21 M. Wood, J. J. Kuo, K. Imasato and G. J. Snyder, *Adv. Mater.*, 2019, **31**, 1902337.
22 K. Imasato, C. Fu, Y. Pan, M. Wood, J. J. Kuo, C. Felser and G. J. Snyder, *Adv. Mater.*, 2020, **32**, 1908218.
23 M. Ozen, A. B. Burcak, D. Zavanelli, M. Heo, M. Yahyaoglu, Y. Oz, U. Burkhardt, H.-S. Kim, G. J. Snyder and U. Aydemir, *ACS Appl. Mater. Interfaces*, 2024, **16**, 52501–52514.
24 M. T. Dylla, J. J. Kuo, I. Witting and G. J. Snyder, *Adv. Mater. Interfaces*, 2019, **6**, 1900222.
25 T. Luo, D. Mangelinck, F. Serrano-Sánchez, C. Fu, C. Felser and B. Gault, *Acta Mater.*, 2022, **226**, 117604.
26 X. Zhang, S. Li, B. Zou, P. Xu, Y. Song, B. Xu, Y. Wang, G. Tang and S. Yang, *J. Alloys Compd.*, 2022, **901**, 163686.
27 Q. Qiu, Y. Liu, K. Xia, T. Fang, J. Yu, X. Zhao and T. Zhu, *Adv. Energy Mater.*, 2019, **9**, 1803447.
28 J. U. Rahman, S. Guo, N. Pérez, K. Jang, C. Jung, P. Ying, C. Scheu, D. Zavanelli, S. Zhang, A. Sotnikov, G. J. Snyder, J. van den Brink, K. Nielsch and R. He, *Adv. Energy Mater.*, 2025, **15**, 2404243.
29 D. Zavanelli, E. Isotta, R. Bueno Villoro, S. Zhang, C. Scheu, S. Bux and G. Snyder, *J. Materiomics*, 2025, **11**, 101116.
30 R. Bueno Villoro, M. Wood, T. Luo, H. Bishara, L. Abdellaoui, D. Zavanelli, B. Gault, G. J. Snyder, C. Scheu and S. Zhang, *Acta Mater.*, 2023, **249**, 118816.
31 J. H. Grebenkemper, Y. Hu, D. Barrett, P. Gogna, C.-K. Huang, S. K. Bux and S. M. Kauzlarich, *Chem. Mater.*, 2015, **27**, 5791–5798.
32 C. J. Perez, M. Wood, F. Ricci, G. Yu, T. Vo, S. K. Bux, G. Hautier, G.-M. Rignanese, G. J. Snyder and S. M. Kauzlarich, *Sci. Adv.*, 2021, **7**, eabe9439.
33 L. Borgsmiller and G. J. Snyder, *J. Mater. Chem. A*, 2024, **12**, 26064–26075.
34 L. Borgsmiller, Q. Li, M. Y. Toriyama and G. J. Snyder, *Adv. Energy Mater.*, 2023, **13**, 2300393.
35 K. A. Borup, K. F. F. Fischer, D. R. Brown, G. J. Snyder and B. B. Iversen, *Phys. Rev. B*, 2015, **92**, 045210.
36 C. Wood, D. Zoltan and G. Stapfer, *Rev. Sci. Instrum.*, 1985, **56**, 719–722.
37 V. Ravi, S. Firdosy, T. Caillat, E. Brandon, K. Van Der Walde, L. Maricic and A. Sayir, *J. Electron. Mater.*, 2009, **38**, 1433–1442.
38 M. Schaffer, B. Schaffer and Q. Ramasse, *Ultramicroscopy*, 2012, **114**, 62–71.
39 S. Zhang and C. Scheu, *Microscopy*, 2017, **67**, i133–i141.
40 A. Jain, S. P. Ong, G. Hautier, W. Chen, W. D. Richards, S. Dacek, S. Cholia, D. Gunter, D. Skinner, G. Ceder and K. A. Persson, *APL Mater.*, 2013, **1**, 011002.

41 L. Borgsmiller, M. Y. Toriyama and G. J. Snyder, *Chem. Mater.*, 2024, **36**, 5542–5551.
42 A. He, S. K. Bux, Y. Hu, D. Uhl, L. Li, D. Donadio and S. M. Kauzlarich, *Chem. Mater.*, 2019, **31**, 8076–8086.
43 J. J. Kuo, M. Wood, T. J. Slade, M. G. Kanatzidis and G. J. Snyder, *Energy Environ. Sci.*, 2020, **13**, 1250–1258.
44 J. P. Heremans and J. Martin, *Nat. Mater.*, 2024, **23**, 18–19.
45 A. Zevalkink, D. M. Smiadak, J. L. Blackburn, A. J. Ferguson, M. L. Chabinyc, O. Delaire, J. Wang, K. Kovnir, J. Martin, L. T. Schelhas, T. D. Sparks, S. D. Kang, M. T. Dylla, G. J. Snyder, B. R. Ortiz and E. S. Toberer, *Applied Physics Reviews*, 2018, **5**, 021303.
46 H.-S. Kim, Z. M. Gibbs, Y. Tang, H. Wang and G. J. Snyder, *APL Mater.*, 2015, **3**, 041506.
47 K. A. Borup, J. de Boor, H. Wang, F. Drymiotis, F. Gascoin, X. Shi, L. Chen, M. I. Fedorov, E. Müller, B. B. Iversen and G. J. Snyder, *Energy Environ. Sci.*, 2015, **8**, 423–435.
48 G. J. Snyder, A. H. Snyder, M. Wood, R. Gurunathan, B. H. Snyder and C. Niu, *Adv. Mater.*, 2020, **32**, 2001537.
49 E. Isotta, M. Y. Toriyama, A. H. Adekoya, E. Shupp, G. J. Snyder and A. Zevalkink, *Mater. Today Phys.*, 2023, **31**, 100967.
50 E. Isotta, S. Jiang, R. Bueno-Villoro, R. Nagahiro, K. Maeda, D. A. Mattlat, A. R. Odufisan, A. Zevalkink, J. Shiomi, S. Zhang, C. Scheu, G. J. Snyder and O. Balogun, *Adv. Funct. Mater.*, 2024, **34**, 2405413.
51 J. J. Kuo, Y. Yu, S. D. Kang, O. Cojocaru-Mirédin, M. Wuttig and G. J. Snyder, *Adv. Mater. Interfaces*, 2019, **6**, 1900429.
52 X. Zheng, A. Li, S. Liu, Z. Han, M. Zhang, F. Liu, C. Fu and T. Zhu, *Acta Mater.*, 2023, **260**, 119346.
53 A. Duparchy, H. Naithani, S. Ghosh, M. Parzer, F. Garmroudi, E. Müller and J. de Boor, *Energy Mater.*, 2025, **5**, year.
54 S. Ghosh, M. Abdelbaky, W. Mertin, E. Müller and J. de Boor, *ACS Appl. Mater. Interfaces*, 2024, **16**, 48619–48628.
55 T. Luo, J. J. Kuo, K. J. Griffith, K. Imasato, O. Cojocaru-Mirédin, M. Wuttig, B. Gault, Y. Yu and G. J. Snyder, *Adv. Funct. Mater.*, 2021, **31**, 2100258.
56 M. M. A. Malki, G. J. Snyder and D. C. Dunand, *Int. Mater. Rev.*, 2023, **68**, 1050–1074.
57 M. Jiang, Q. Zhang, S. Zhang, M. Liu, Y. Fu, Z. Zhang, X. Ai, B. Mortazavi, L. Wang, Q. Zhang, D. Makarov and W. Jiang, *Nat. Commun.*, 2025, **16**, 7592.
58 M. Al Malki, Q. Qiu, T. Zhu, G. Snyder and D. Dunand, *Mater. Today Phys.*, 2019, **9**, 100134.
59 Z. C. Cordero, B. E. Knight and C. A. Schuh, *Int. Mater. Rev.*, 2016, **61**, 495–512.
60 J. P. Male, B. Hogan, M. Wood, D. Cheikh, G. J. Snyder and S. K. Bux, *Mater. Today Phys.*, 2023, **32**, 101016.